Role of Geometric Shape in Chiral Optics: supplementary material

Philipp Gutsche[1,2], Xavier Garcia-Santiago[3], Philipp-Immanuel Schneider[4], Kevin M. McPeak[5], Manuel Nieto-Vesperinas[6], and Sven Burger[2,4]

[1]Freie Universität Berlin, Mathematics Institute, 14195 Berlin, Germany
[2]Zuse Institute Berlin, Computational Nano Optics, 14195 Berlin, Germany
[3]Karlsruhe Institute of Technology, Institut für Theoretische Festkörperphysik, 76131 Karlsruhe, Germany
[4]JCMwave GmbH, 14050 Berlin, Germany
[5]Lousiana State University, Department of Chemical Engineering, Baton Rouge, LA
[6]Instituto de Ciencia de Materiales de Madrid, Consejo Superior de Investigaciones Científicas, Madrid, 28049, Spain

Abstract

This document provides supplementary information to the article entitled 'Role of Geometric Shape in Chiral Optics'. The Vector Spherical Harmonics as basis functions for the T-matrix and the T-matrix itself are summarized. Transformations of T as well as mirror planes in T and numerical inaccuracies are discussed. Further, the symmetry classes shown in the main article are analyzed in the dipolar approximation and the physical relevance of the chosen 2-norm for the optical chirality coefficient χ_{TT} is outlined. Addtionally, we explain the exact geometric model of the helix and the construction of the geometric chirality coefficient χ_{GE}. Finally, details on the minimization procedure, which is obtained with Bayesian Optimization, are given.

1 Vector Spherical Harmonics

The solution of Maxwell's equations for an isolated scatterer being the subject to external illumination is conventiently expressed in the basis of vector spherical harmonics (VSHs) $\boldsymbol{N}_{nm}^{(l)}(\boldsymbol{x})$ and $\boldsymbol{M}_{nm}^{(l)}(\boldsymbol{x})$ [7]. The index n is the multipole

order and is related to the eigenvalue $n(n+1)$ of the squared orbital angular-momentum operator L^2. The index m is the eigenvalue of the z-component of the orbital angular-momentum operator L_z [6, Sec. 9.7,]. The superscript l differentiates between incident ($l = 1$) and scattered ($l = 3$) electromagnetic fields.

In the VSH basis, the incident electric $\boldsymbol{\mathcal{E}}_{\mathrm{inc}}$ and magnetic $\boldsymbol{\mathcal{H}}_{\mathrm{inc}}$ time-harmonic fields are

$$\boldsymbol{\mathcal{E}}_{\mathrm{inc}}(\boldsymbol{x},t) = e^{-i\omega t}\sum_{n=1}^{\infty}\sum_{m=-n}^{m=n} p_{mn}\boldsymbol{N}_{mn}^{(1)}(\boldsymbol{x}) + q_{mn}\boldsymbol{M}_{mn}^{(1)}(\boldsymbol{x}), \tag{1}$$

$$\boldsymbol{\mathcal{H}}_{\mathrm{inc}}(\boldsymbol{x},t) = -\frac{ie^{-i\omega t}}{Z}\sum_{n=1}^{\infty}\sum_{m=-n}^{m=n} p_{mn}\boldsymbol{M}_{mn}^{(1)}(\boldsymbol{x}) + q_{mn}\boldsymbol{N}_{mn}^{(1)}(\boldsymbol{x}), \tag{2}$$

with the wave impedance $Z = \sqrt{\mu_0\mu/(\varepsilon_0\varepsilon)}$ and the relative permeability μ and relative permittivity ε of the surrounding medium. The scattered fields obeying the radiation condition are given by

$$\boldsymbol{\mathcal{E}}_{\mathrm{sca}}(\boldsymbol{x},t) = e^{-i\omega t}\sum_{n=1}^{\infty}\sum_{m=-n}^{m=n} a_{mn}\boldsymbol{N}_{mn}^{(3)}(\boldsymbol{x}) + b_{mn}\boldsymbol{M}_{mn}^{(3)}(\boldsymbol{x}), \tag{3}$$

$$\boldsymbol{\mathcal{H}}_{\mathrm{sca}}(\boldsymbol{x},t) = -\frac{ie^{-i\omega t}}{Z}\sum_{n=1}^{\infty}\sum_{m=-n}^{m=n} a_{mn}\boldsymbol{M}_{mn}^{(3)}(\boldsymbol{x}) + b_{mn}\boldsymbol{N}_{mn}^{(3)}(\boldsymbol{x}). \tag{4}$$

The VSHs $\boldsymbol{N}_{nm}^{(3)}(\boldsymbol{x})$ and $\boldsymbol{M}_{nm}^{(3)}(\boldsymbol{x})$ are the electric fields due to induced electric and magnetic multipoles, respectively.

2 T-Matrix

The coefficients p_{mn} and q_{mn} as well as a_{mn} and b_{mn} are the VSH coefficients of the incident and scattered field, respectively. The optical response of a scatterer is described by the relation of these two sets of coefficients. Specifically, the T-matrix enables the computation of the scattered field $(\boldsymbol{a},\boldsymbol{b})$ from a known incident field $(\boldsymbol{p},\boldsymbol{q})$, where all coefficients are summarized in vectors:

$$T\begin{pmatrix}\boldsymbol{p}\\ \boldsymbol{q}\end{pmatrix} = \begin{pmatrix}\boldsymbol{a}\\ \boldsymbol{b}\end{pmatrix}. \tag{5}$$

Accordingly, all possible observable quantities such as scattered energy, absorption and chirality extinction can be deduced from the T-matrix [7, 4].

In this study, we analyze quadratic T-matrices of dimension $2N(N+2)$ with maximal multipole order $N = 5$. T is obtained numerically by the illumination with 150 plane waves. The respective incident wave vectors are distributed equidistanly on a spherical surface and the polarizations are chosen randomly. The projection of the scattered field onto VSHs is computed from general surface integrals [2]. The resulting matrices for the extremal CD response (Figure 2 in main text) at $\lambda = 823$nm and $\lambda = 1,452$nm are shown in Figure 1.

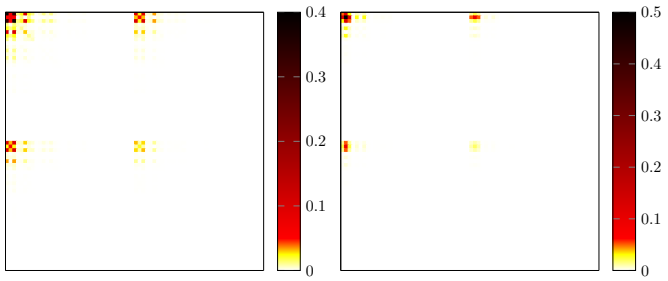

Figure 1: Colorplot of absolute values of the T-matrix entries at $\lambda = 823$nm (left) and $\lambda = 1,452$nm (right) which correspond to extremal values in the CD spectrum.

3 Transformation of T

The T-matrix is useful for transformations R such as rotating $\mathcal{R}$, translating $\mathcal{T}$ and mirroring $\mathcal{M}$ the object of interest. Under mirror reflection $\mathcal{M}_{xy}$ on the xy-plane, both the incident ($l = 1$) and the scattered ($l = 3$) VSHs transform as

$$(\mathcal{M}_{xy}\boldsymbol{N}_{mn}^{(l)})(\boldsymbol{x}) = (-1)^{(m+n)}\boldsymbol{N}_{mn}^{(l)}(\boldsymbol{x}), \tag{6}$$

$$(\mathcal{M}_{xy}\boldsymbol{M}_{mn}^{(l)})(\boldsymbol{x}) = (-1)^{(m+n+1)}\boldsymbol{M}_{mn}^{(l)}(\boldsymbol{x}). \tag{7}$$

Accordingly, the matrix T_l representing the mirror image of the scatterer with T-matrix T_r is given by

$$T_l = \mathcal{M}_{xy}^{-1} T_r \mathcal{M}_{xy}, \tag{8}$$

with $(\mathcal{M}_{xy})_{ij} = (-1)^{(m+n)}\delta_{ij}$ for $i = 1, ..., N(N+2)$ and with $(\mathcal{M}_{xy})_{ij} = (-1)^{(m+n+1)}\delta_{ij}$ for $i = N(N+2)+1, ..., 2N(N+2)$.

By employing the addition theorems for translation $\mathcal{T}$ and rotation $\mathcal{R}$ of VSHs [10], the T-matrix of the transformed scatterer is computed analytically. Note that the mirrored and rotated T-matrices are exact, whereas the translated T-matrix is an approximation due to the finite size of T, i.e. the maximal multipole order $N = 5$. In Figure 2, we plot the error Δ of forward and backward translation in the same direction with $\Theta = 76°, \Phi = 330°$ and $d = 206$nm. Although the scatterer is mapped onto its original position, the truncation of T introduces the error

$$\Delta = \frac{\max_{ij}\left|\left(T_r - \mathcal{T}_{\text{back}}^{-1}\left\{\mathcal{T}_{\text{forw}}^{-1} T_r \mathcal{T}_{\text{forw}}\right\}\mathcal{T}_{\text{back}}\right)_{ij}\right|}{\max_{ij}\left|(T_r)_{ij}\right|}. \tag{9}$$

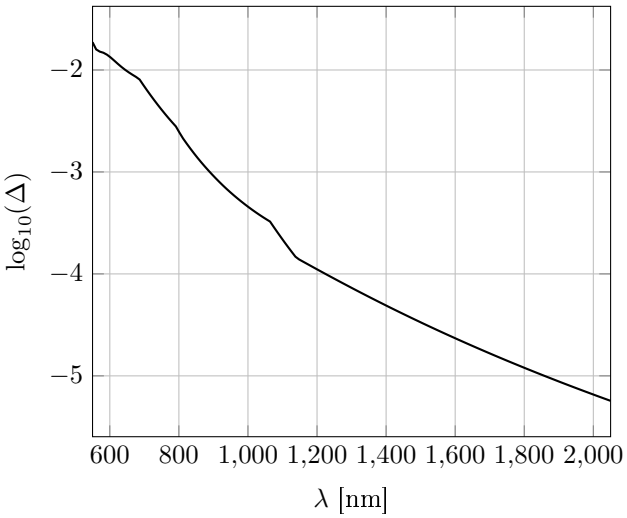

Figure 2: Numerical error of translation due to the finite size of T with maximal multipole order $N = 5$.

4 Mirror Planes in T

As discussed in the main text, the aim of this study is to find symmetries in T which correspond to geometric mirror planes, or at least identifying planes of highest possible mirror symmetry for which the T-matrices of the original scatterer and its mirror image show the highest similarity. This is done by the global minimization in Eq. (3). As illustrative examples, we show the angle-dependent, i.e. non-minimized, $\chi_{\mathrm{TT}}(\Theta, \Phi, 0)$ for rotations by angles Θ and Φ without translation ($d = 0$), in Figure 3. All possible rotations of two matrices at the extremal values of the CD spectrum are shown (cf. Figure 1) with

$$\chi_{\mathrm{TT}}(\Theta, \Phi, d) = \left|\left|T_l - R^{-1}(\Theta, \Phi, d) T_r R(\Theta, \Phi, d)\right|\right|_2 . \tag{10}$$

It is apparent in the change of similarity planes (Figure 3 in main text) and the angular dependence of the similarity of the T-matrices of mirror images (Figure 3) that the symmetry of T is highly wavelength dependent. This is due to the fact that for shorter wavelengths, higher multipoles contribute to the overall response as shown in Figure 4. There, we show the absolute value of the T-matrix entries which correspond to averaged electric and magnetic multipole orders $N = 1$ (dipole) and $N = 2$ (quadrupole). Overall the response is dominated by electric dipole contributions. Below $\lambda = 1\mu$m, magnetic dipole and electric quadrupole effects are increasing and result in symmetry planes which are not found in a purely geometric analysis.

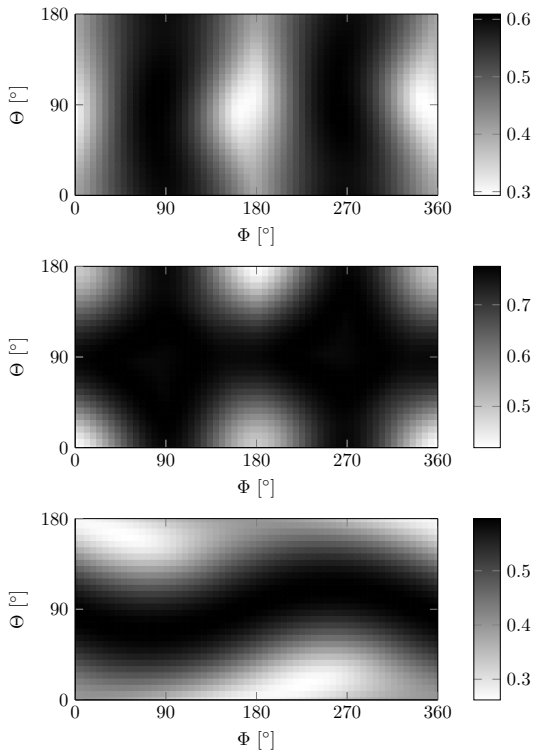

Figure 3: $\chi_{\mathrm{TT}}(\Theta, \Phi, 0)$ is the norm of the difference between original T-matrix and the matrix of a mirrored scatterer rotated by Θ and Φ around the centroid of the helix for $\lambda = 623$nm (top), $\lambda = 823$nm (middle) and $\lambda = 1,452$nm (bottom).

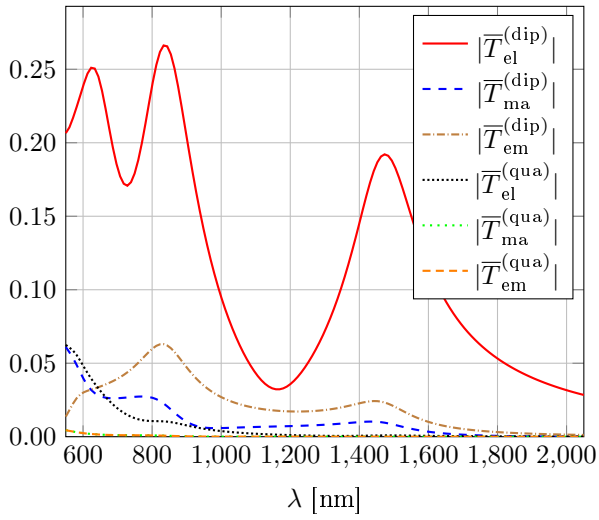

Figure 4: Absolute value of averaged entries of T corresponding to electric, magnetic and electric-magnetic dipole and quadrupole moments.

5 Dipolar Analysis of Symmetry Classes

In order to investigate the physical origin of the three symmetry classes found in our analysis, we further study the T-matrix in the dipolar approximation, i.e. the electric $T^{(\mathrm{dip})}_{\mathrm{el}}$, the magnetic $T^{(\mathrm{dip})}_{\mathrm{ma}}$ and the electric-magnetic part $T^{(dip)}_{\mathrm{em}}$. These matrices are often the dominant contribution (cf. Fig. 1) and are defined as follows:

$$T = (T_{ij})_{i,j=1,\ldots,2N(N+2)} \tag{11}$$

$$T^{(\mathrm{dip})}_{\mathrm{el}} = (T_{ij})_{i,j=1,\ldots,3} \tag{12}$$

$$T^{(\mathrm{dip})}_{\mathrm{ma}} = (T_{ij})_{i,j=N(N+2)+1,\ldots,N(N+2)+3} \tag{13}$$

$$T^{(\mathrm{dip})}_{\mathrm{em}} = (T_{ij})_{i=1,\ldots,3;\ j=N(N+2)+1,\ldots,N(N+2)+3}\,. \tag{14}$$

For each 3x3 matrix, we compute the three eigenvalues $\alpha_{\boldsymbol{v}}$ with e.g. $T^{(\mathrm{dip})}_{\mathrm{el}}\boldsymbol{v} = \alpha_{\boldsymbol{v}}\boldsymbol{v}$. In Fig. 5, we show the absolute value of $\alpha_{\boldsymbol{v}}$ as well as the spherical coordinates $\Theta_{\boldsymbol{v}}$ and $\Phi_{\boldsymbol{v}}$ of the respective eigenvector.

The quantities belonging to the largest eigenvalue are plotted with large black circles. The second largest eigenvalue is depicted with small black circles and the smallest one has small gray circles. The y-axis of $|\alpha_{\boldsymbol{v}}|$ is presented on the left and the y-axis for the two angles is placed on the right. Alongside the x-axis, the colored wavelength-dependent symmetry classes found in our study are shown. The transitions between these classes at $\lambda = 680$nm and $\lambda = 1025$nm are shown with gray vertical lines.

The transitions between the symmetry classes occur for a change in the dominant eigenvalue of the electric, magnetic and electric-magnetic submatrices, i.e. for different resonances of the scatterer. That is why the symmetry planes discussed in the main text are sharply separated. There is always a smooth line connecting the parameters of the eigenvalues, however, the dominant eigenstate is highly wavelength-dependent and introduces the drastic changes in the symmetry of T.

Note that the changes of the maximal eigenvalue do not exactly coincide for the electric, magnetic and electric-magnetic matrices. This illustrates that the symmetry of T and especially the chiral behaviour of the helix is dependent on a complex interplay between electric and magnetic contributions as well as higher order multipoles which are not shown here. In comparison with the multipolar resonance behavior, the scalar coefficient χ_{TT} introduced in the main text largely simplifies the analysis of the chiral behavior of the scatterer.

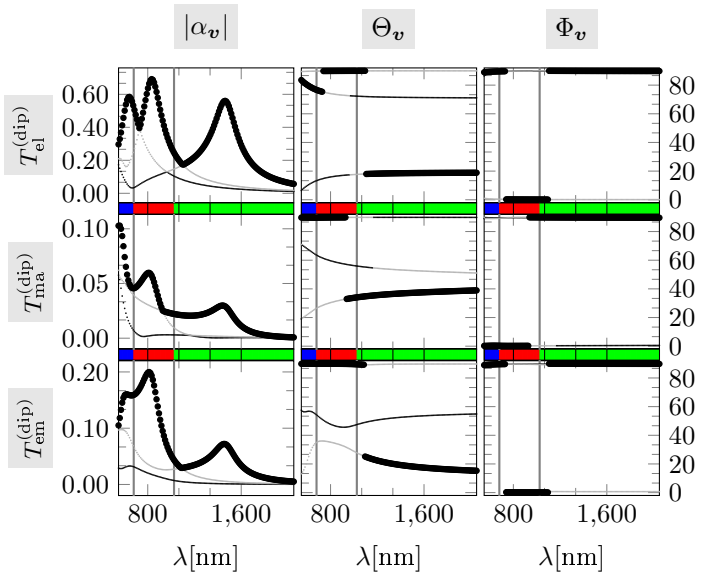

Figure 5: Eigenvalue analysis of dipolar contributions. See section on dipolar analysis for details.

6 Physical Relevance of the 2-norm

The electromagnetic chirality coefficient χ_{CD} is directly accessible by experiment: it is the differential energy extinction due to the illumination by right and left handed circularly polarized plane waves. The observed energy extinctions at different angles of incidence (Θ, Φ) are averaged over the whole solid angle. Numerically, this quantity is deduced from the T-matrix which contains

the full angular- and polarization-resolved optical response of the scatterer [4, Eq. (27)].

For the coefficient χ_{SV} the T-matrix itself is analyzed rather than the experimentally measurable quantities in the experiment. Here, the ability of retrieving the full optical response by illumination with fields of only one state of well-defined helicity is quantified [1]. Irrespective of any particular conditions of the incident field and/or the experimental observables, a general property of the scattering object is obtained, namely, whether the scatterer is electromagnetically chiral. The latter property is introduced in Ref. [1].

In the current study, we put forward a concept relating the geometric property of (a)chirality of an object to its optical properties. Specifically, we find planes of similarity in the T-matrix which directly relate to geometric mirror planes. For simplicity, we choose the 2-norm $||\cdot||_2$ in Eq. (3) in the main text. Depending on the experimental setup, other matrix norms or operations may be chosen which correspond to observables such as the scattered chirality [5]. In any case, the measurable quantity can be computed from the T-matrix since all optical information is contained therein.

For the specific choice of the 2-norm, not only the geometric mirror plane of highest similarity between mirror images is obtained. Further, the required illumination parameters are given directly. We recall that the 2-norm of any matrix A is its maximal singular value $\sigma_{\max}$: $||A||_2 = \sigma_{\max}(A)$. Additionally, the singular value decomposition is a factorization of A into $A = U\Sigma V^*$ with the diagonal matrix of singular values Σ and unitarity matrices U and V. The matrices U and V consist of the left- $\boldsymbol{u}$ and right-singular vectors $\boldsymbol{v}$ of singular value σ with

$$A\boldsymbol{v} = \sigma\boldsymbol{u}. \tag{15}$$

Note that due to the unitarity of U and V, the singular vectors are normalized: $||\boldsymbol{u}||_2 = ||\boldsymbol{v}||_2 = 1$.

In Eq. (3) in the main text, the difference of the matrices T_l and T_r of the (transformed) mirror images are compared. Accordingly, it holds $\chi_{\mathrm{TT}} = \sigma_{\max}(T_r - R^{-1}T_lR)$, where we omit the rotation and translation parameters (Θ, Φ, d). The singular value decomposition gives the VSHs coefficients of the incident field with minimal χ_{TT} as $\boldsymbol{v}_{\max} = (\boldsymbol{p}_{\max}, \boldsymbol{q}_{\max})$ with

$$\chi_{\mathrm{TT}} = \left|\left|(T_r - R^{-1}T_lR)\begin{pmatrix} p_{\max} \\ q_{\max} \end{pmatrix}\right|\right|_2 = W_{\mathrm{sca}}(T_r - R^{-1}T_lR). \tag{16}$$

The last step is fulfilled since the absolute value of the scattered VSH coefficients is proportional to the scattered energy [7] i.e. $W_{\mathrm{sca}}(T_r - R^{-1}T_lR)$ is the integrated scattered energy flux of the matrix $T_r - R^{-1}T_lR$ with an incident field given by $(p_{\max}, q_{\max})$ [5, Eq. (6)]. Accordingly, the coefficient χ_{TT} is proportional to the scattered energy of the differential field due to the (transformed) mirror images T_r and $R^{-1}T_lR$ with the smallest discrepancy. Note that this discussion does not correspond to the scattering problem with both the right- (T_r) and transformed left-handed enantiomers (R^1T_lR) since multiple scattering

of both objects [11] is omitted. It rather illustrates the relevance of the 2-norm and its relation to the physically observable scattered energy W_{sca}.

The respective geometric parameters $(\Theta_{\min}, \Phi_{\min}, d_{\min})$ of χ_{TT} follow from the optimization parameters. Accordingly, we obtain in our approach both the incident field (from its VSH coefficients) as well as the mirror plane (from its parameters) corresponding to an experimental realizable setup.

7 Electromagnetic Chirality Coefficient

The electromagnetic chirality coefficient χ_{SV} is based on the singular-value decomposition of the T-matrix in the helicity basis [1]. The T-matrix in the helicity basis $T_{\mathcal{H}}$ is given as

$$T_{\mathcal{H}} = \frac{1}{2} \begin{pmatrix} \mathbb{1} & \mathbb{1} \\ \mathbb{1} & -\mathbb{1} \end{pmatrix} T \begin{pmatrix} \mathbb{1} & \mathbb{1} \\ \mathbb{1} & -\mathbb{1} \end{pmatrix}, \tag{17}$$

$$T_{\mathcal{H}} = \begin{pmatrix} T_{\mathcal{H}}^{++} & T_{\mathcal{H}}^{+-} \\ T_{\mathcal{H}}^{-+} & T_{\mathcal{H}}^{--} \end{pmatrix}. \tag{18}$$

With the singular values $\sigma(A)$ of matrix A, the vectors

$$\sigma^{+} = \left(\sigma(T_{\mathcal{H}}^{++}), \sigma(T_{\mathcal{H}}^{-+})\right), \tag{19}$$

$$\sigma^{-} = \left(\sigma(T_{\mathcal{H}}^{--}), \sigma(T_{\mathcal{H}}^{+-})\right) \tag{20}$$

are used to compute the electromagnetic chirality coefficient χ_{SV}:

$$\chi_{\mathrm{SV}} = \sqrt{\frac{\sum_{i=1}^{N(N+2)} \left(\sigma_i^{+} - \sigma_i^{-}\right)^2}{\sum_{i=1}^{N(N+2)} \left(\sigma_i^{+}\right)^2 + \left(\sigma_i^{-}\right)^2}}. \tag{21}$$

As described in the main text, the coefficient χ_{SV} shows different behaviour compared to the observable CD spectrum χ_{CD}. χ_{SV} is normalized by the average interaction strength. However, this normalization is not the only reason for the discrepancy of χ_{SV} and χ_{CD}. In Fig. 6, we show the normalized CD spectrum, i.e. the g-factor, compared to the former two coefficients. This shows that the singular-value decomposition involved in the computation of χ_{SV} yields non-smooth behaviour of $\chi_{\mathrm{SV}}(\lambda)$.

8 Geometric Model

The analyzed object is a gold helix with paramters taken from Ref. [12]. The permittivity of Au is derived from a fit of experimental data to a Lorentz-Drude model [8].

In Fig. 7, the construction of the helix based on a CAD-model is shown. Two spheres with radius of 35nm are placed at the top and bottom of a cylinder with radius of 60nm and height of 230nm. This yields $z = \pm 115$nm and $x = 60$nm

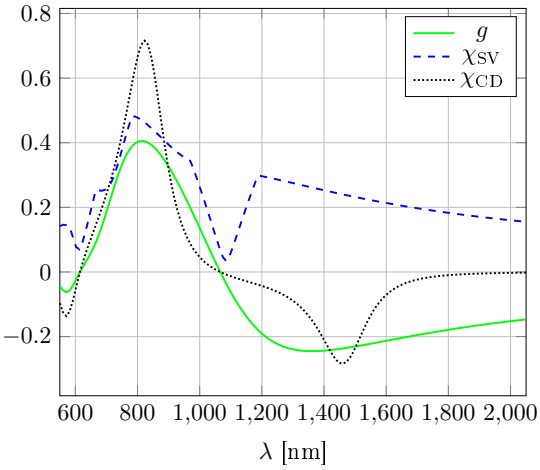

Figure 6: Comparison of χ_{SV}, χ_{CD} and the g-factor.

for the upper and lower sphere, respectively. A circle of radius 35nm is swept along a path on the cylindrical surface. Due to numerical stability, the path is divided into six segments. This procedure results in a helix with one coil and a circular cross section.

9 Geometric Chirality Coefficient

Similar to the approach of finding mirror planes in the T-matrix, mirror planes in a geometric object may be found by analyzing the overlap of the original object O_r and its mirror image O_l. The mirror image O_l is rotated by (Θ, Φ) and translated from its centroid by the distance d in order to maximize the overlap with the original object O_r. In Fig. 8, we depict the original helix in grey and its rotated mirror image in blue. The overlap $O_l \cap O_r$ is shown in red.

For the geometric chirality coefficient χ_{GE}, the volume of the overlap $V(O_r \cap O_l)$ is maximized and given in units of the original volume $V(O_r)$ [Eq. (4) in the main text and Ref. [3]]. Since the mirror image of an achiral object may be brought to complete overlap, the coefficient vanishes in the achiral case: $\chi_{\mathrm{GE}} = 0$. By contrast, if the mirror image does not overlap at all, the coefficient equals unity. Note, however, that there exists an overlap for any (including chiral) object. Accordingly, $\chi_{\mathrm{GE}} = 1$ is only a theoretical value.

In Figure 3 in the main text, the coefficient $\chi_{\mathrm{GE}}(\Theta, \Phi, 0)$, which depends on the rotation angles, is shown. The relevant scalar, is the minimum of this coefficient as it occurs for the maximal overlap. Including translations in $\chi_{\mathrm{GE}}(\Theta, \Phi, d)$, it is always possible to obtain $\chi_{\mathrm{GE}}(\Theta, \Phi, d) = 1$ by translating the mirror images out of their respective bounding boxes. Only the analysis of all possible rotations and translations (i.e. the minimization procedure) yields

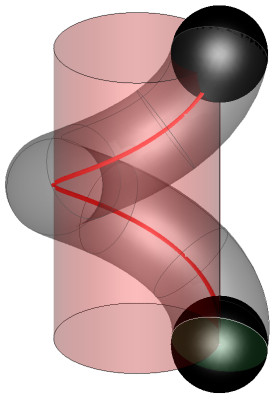

Figure 7: Construction of helix: Spheres (black) are placed at the top and bottom. A circle (green) is swept along a line (red) on the cylindrical surface (red, transparent). The helix (grey, transparent) consists of six parts in parameter space.

a relevant coefficient which vanishes if the object possesses a mirror plane.

10 Bayesian Optimization

The global minimization of $\chi_{\mathrm{TT}}(\Theta, \Phi, d)$ in Eq. (3) in the main text takes place in a three-dimensional space with parameters defined by the rotations around the angles (Θ, Φ) and the translation by the distance d. Since the behaviour of the similarity of the original T-matrix T_l and the matrix of the transformed mirror image T_r is unknown, a global optimizer is required to obtain the coefficient χ_{TT} providing the highest symmetry in the T-matrix of the helix.

Bayesian Optimization (BO) is a procedure based on a stochastic model given by Gaussian processes (GPs) [9]. The optimization starts at a random point in the parameter space and predicts the objective function in the full space based on the previously obtained values. This stochastic model is used to identify parameter values which yield a large expected improvement with respect to the currently known minimum. Subsequently, the function value of the point with the highest expected improvement is determined and the predictive model is refined. Different stopping criteria such as the maximum number of function evaluations, the smallest probability of improvement or the smallest expected improvement are possible.

In the current study, we use a maximum number of 500 function evaluations, a minimal probability of improvement of 10^{-6} and a minimal expected improvement of 10^{-5}. The latter criterion is based on the numerical accuracy which is limited by the translation addition theorem for a finite T-matrix (cf. Fig. 2). Further, we parametrize the space (Θ, Φ, d) as follows in order to obtain parameters $(p_1, p_2, p_3) \in [0, 1]^3$ and shift physical significant points such as the

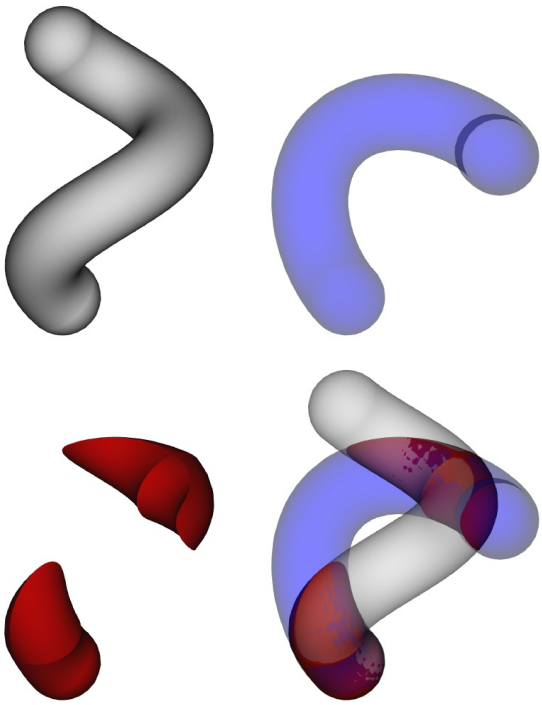

Figure 8: Overlap (red) of the original helix (grey) and the transformed helix (blue) which is mirrored and rotated around the y-axis with $\Theta = 125°$ yielding the maximal overlap with $\chi_{\mathrm{GE}} = 0.57$.

centroid ($d = 0$) to the inner part of the parameter intervals:

$$\Phi = 360^\circ(p_1 - 0.7), \tag{22}$$

$$\Theta = 180^\circ \left(\frac{p_2 - 0.1}{1 - 0.1}\right)^2, \tag{23}$$

$$d = 206\text{nm} \left(\frac{p_3 - 0.2}{1 - 0.2}\right)^2. \tag{24}$$

The parametrizations above are chosen such that no symmetry point corresponds to the boundaries of the parameter space $[0, 1]^3$. The quadratic functions involving p_2 and p_3 introduce ambiguities in the parameter space which are irrelevant for the physical values obtained from the inverse functions

$$p_1 = \frac{\Phi}{360^\circ} + 0.7, \tag{25}$$

$$p_2 = \sqrt{\frac{\Theta}{180^\circ}}(1.0 - 0.1) + 0.1, \tag{26}$$

$$p_3 = \sqrt{\frac{d}{206\text{nm}}}(1.0 - 0.2) + 0.2. \tag{27}$$

The relation between the variables (Θ, Φ, d) and the parameters (p_1, p_2, p_3) is depicted in Fig. 9.

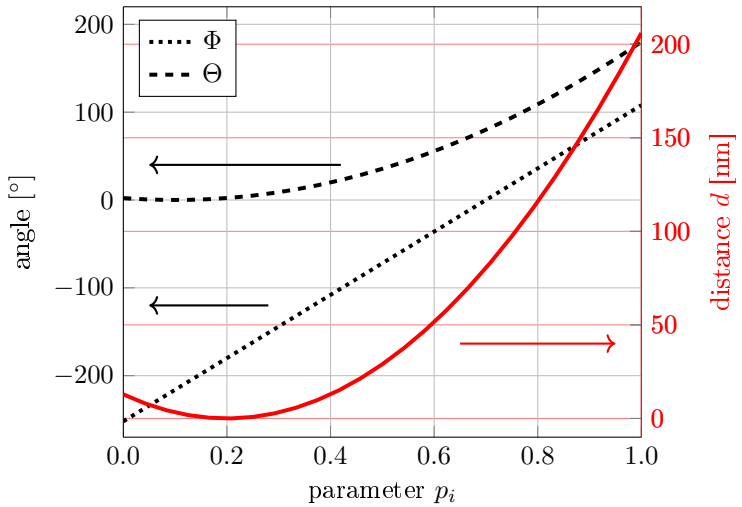

Figure 9: Parametrization for optimization with (p_1, p_2, p_3).

The stochastic nature of the BO enables the predicition of objective values in the full parameter space as well as predicting the uncertainties, i.e. standard deviations, of these values. Accordingly, an interpolation of the parameter space is possible. For the two extrema of the CD, the prediction given by the BO is

shown in Fig. 10. From the respective minimal values of $\chi_{\mathrm{TT}}(p_1^{\min}, p_2^{\min}, p_3^{\min})$ cuts through the parameter space in all three directions are shown. For each cut, one parameter (e.g. p_1) is varied and the other parameters are kept constant (e.g. $p_2 = p_2^{\min}$ and $p_3 = p_3^{\min}$).

As clearly visible, the minima are very flat with respect to parameter p_3, i.e. translation from the centroid. For $\lambda = 823$nm, the minimum is additionally flat for p_2, i.e. rotations by Θ. In other words, small variations in the translation d (and the rotation by Θ in the first case) do not change significantly χ_{TT}. Accordingly, the similarity between the T-matrices of the mirror images do not change when d (and Θ) are varied. That is why, the results of the optimization are subject to ambiguity caused by numerical fluctuations.

The results of the minimization are shown in Fig. 11. These parameters correspond to the planes displayed in Fig. 3. As seen in the latter, the symmetry class 2 is divided into two subclasses: one class for $\lambda \in [600, 680]$nm and a second class for $\lambda \in [550, 600]$nm. These two classes differ only by a roation of 180° about the z-axis.

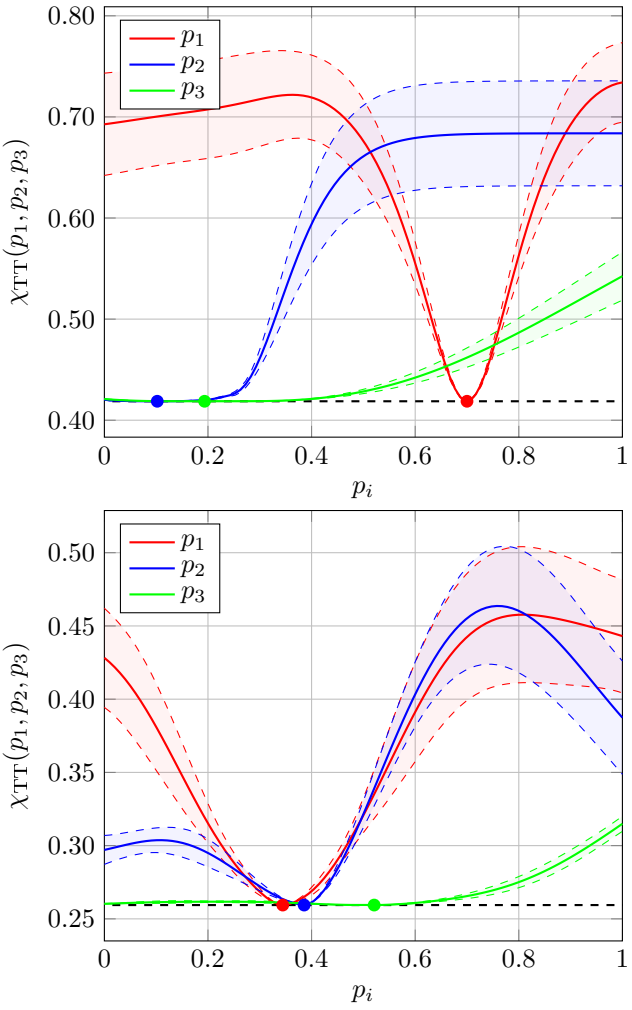

Figure 10: Sensitivity of χ_{TT} for $\lambda = 823$nm (top) and $\lambda = 1,452$nm (bottom). Minimal parameters (dots) and minimal χ_{TT} (black dashed line) are shown. Solid lines are variations of p_1 (red), p_2 (blue) and p_3 (green) from the minimum. Shaded areas depict standard deviation derived from GPs.

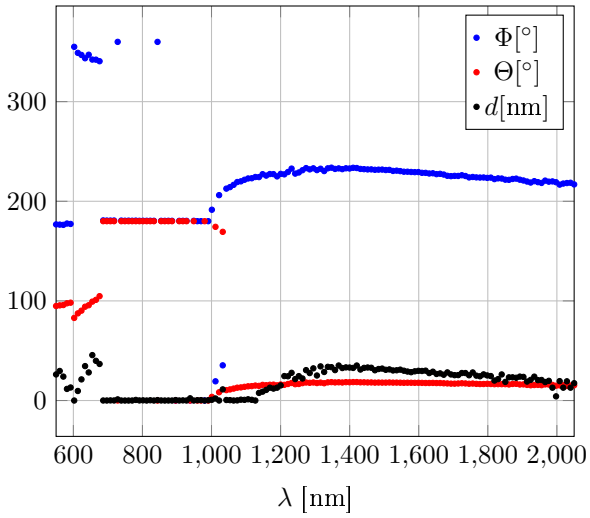

Figure 11: Results of minimization.

11 Achiral Scatterer

In order to verify our approach, we briefly illustrate our method with a achiral scatterer, i.e. an object containing a mirror plane. We use a ellipsoidal body similar to a dielectric sphere with radius 230 nm and refractive index 3.5. The illuminating wavelength is 1800 nm which is roughly within the scattering peak of the magnetic dipole moment (cf. [4]).

The ellipsoidal particle is defined by six numbers being the three principal axes with different values in positive and negative direction of the axis. Namely, the numbers x_1 and x_2 describe the length of the axis in positive (x_1) and negative (x_2) direction of the x-axis. The remaining two axes y and z are defined analogously. The particle is constructed out of eight partial ellipsoids each taking three axes including their direction into account. If all six numbers are chosen distinctively, the particle is chiral without a mirror plane. Here, we choose $x_1 = x_2 = 230$nm yielding a mirror plane in the yz-plane. The remaining dimensions are $y_1 = 184$nm, $y_2 = 253$nm, $z_1 = 276$nm and $z_2 = 207$nm.

In Fig. 12, we show the result of the global minimization of $\chi_{\mathrm{TT}}(\Theta, \Phi, d)$ and its relation to the geometric chirality coefficient χ_{GE}. It is apparent that the expected mirror plane is found up to numerical accuracy. After 81 steps the minimization obtains $\chi_{\mathrm{TT}} \approx 0.0052$ with the angles $\Phi \approx 359.0196$ and $\Theta = 180$. The displacement from the theoretically expected centroid is 0.1126 nm. This shows that our approach finds the mirror plane for a achiral scatterer within the T-matrix as expected.

The optimization steps undertaken by the Bayesian Optimization is displayed in Fig. 13. The maximal value obtained in the inspected domain is $\chi_{\mathrm{TT}} \approx 0.1606$. The parametrization described in the previous section with normalized parameters p_1, p_2 and p_3 shows that the whole design space is analyzed by the optimizer. Note that from the history of the minimization further analysis is possible by estimating the objective value for non-computed points in parameter space with the help of Gaussian processes [9].

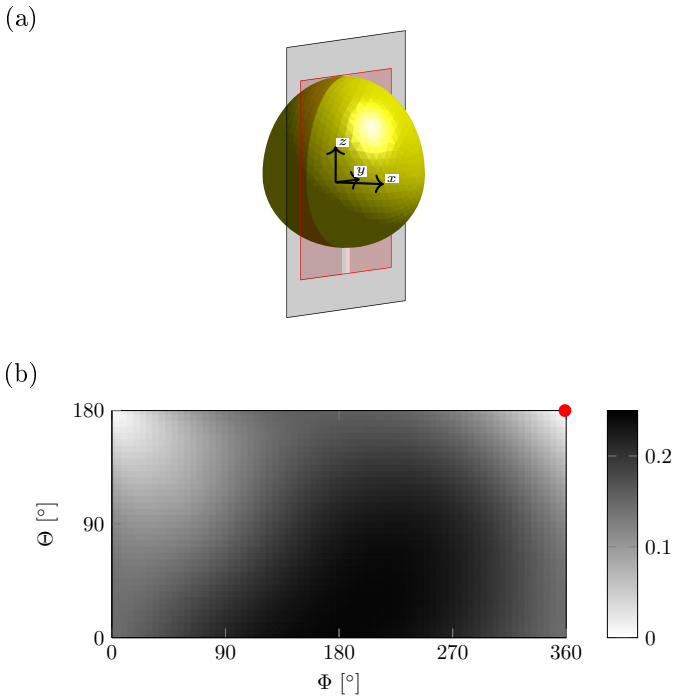

Figure 12: (a) Transformed xy-plane (red) corresponding to minimal χ_{TT} computed from T-matrix of the achiral scatterer (yellow). The plane is computed for a incident wavelenght $\lambda = 1800$nm. The dark grey plane corresponds to minimal χ_{GE}. (b) Geometric chiral coefficient $\chi_{\mathrm{GE}}(\Theta, \Phi)$ for the scatterer and its mirror image which is rotated around the centroid (grey colormap). The minimal value of 0.0 belongs to the dark grey plane in Fig. 12(a). The angles of the red plane is shown by a red circle.

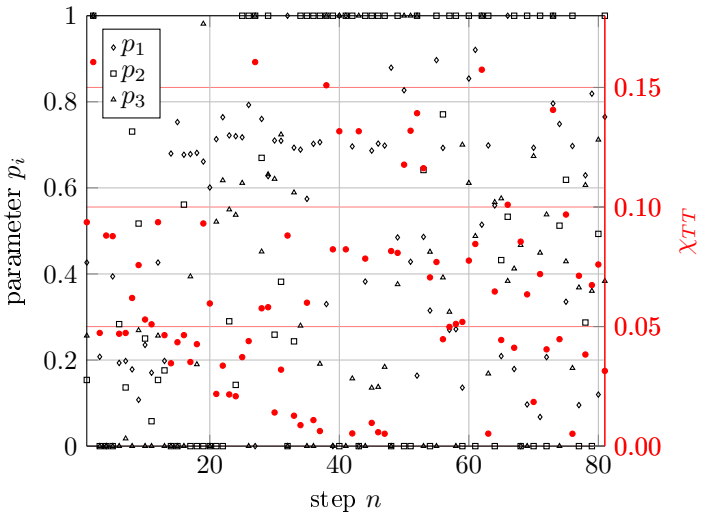

Figure 13: Minimization for obtaining χ_{TT} for the achiral ellipsoidal scatterer. The analyzed normalized parameters are shown in black and the obtained values for χ_{TT} are given in red. The whole parameter space is investigated before the optimizer terminates after 81 steps.

References

[1] I. Fernandez-Corbaton, M. Fruhnert, and C. Rockstuhl. Objects of maximum electromagnetic chirality. *Phys. Rev. X*, 6(3):031013, 2016.

[2] X. Garcia Santiago, M. Hammerschmidt, S. Burger, C. Rockstuhl, I. Fernandez Corbaton, and L. Zschiedrich. Decomposition of scattered electromagnetic fields into vector spherical wave functions on surfaces with general shapes. *Physical Review B*, 99(4):045406, 2019.

[3] G. Gilat. On quantifying chirality - obstacles and problems towards unification. *J. Math. Chem.*, 15(1):197–205, 1994.

[4] P. Gutsche and M. Nieto-Vesperinas. Optical chirality of time-harmonic wavefields for classification of scatterer. *Sci. Rep.*, 8:9416, 2018.

[5] P. Gutsche, P.-I. Schneider, S. Burger, and M. Nieto-Vesperinas. Chiral scatterers designed by bayesian optimization. *J. Phys.: Conf. Ser.*, 963:012004, 2018.

[6] J. D. Jackson. *Classical Electrodynamics*. John Wiley and Sons, 3rd edition, 1998.

[7] M. Mishchenko, L. Travis, and A. Lacis. *Scattering, Absorption, and Emission of Light by Small Particles*. Cambridge University Press, 2002.

[8] A. D. Rakić, A. B. Djurišić, J. M. Elazar, and M. L. Majewski. Optical properties of metallic films for vertical-cavity optoelectronic devices. *Appl. Opt.*, 37(22):5271–5283, 1998.

[9] P.-I. Schneider, X. G. Santiago, C. Rockstuhl, and S. Burger. Global optimization of complex optical structures using bayesian optimization based on gaussian processes. *Proc. SPIE 10335*, 10335:103350O, 2017.

[10] S. Stein. Addition theorems for spherical wave functions. *Quarterly of Applied Mathematics*, 19(1):15–24, 1961.

[11] D. Theobald, A. Egel, G. Gomard, and U. Lemmer. Plane-wave coupling formalism for t-matrix simulations of light scattering by nonspherical particles. *Physical Review A*, 96(3):033822, 2017.

[12] P. Wozniak, I. De Leon, K. Höflich, C. Haverkamp, S. Christiansen, G. Leuchs, and P. Banzer. Chiroptical response of a single plasmonic nanohelix. *Optics express*, 26(15):19275–19293, 2018.